Research Article | Vol. 33, No. 21 / 20 Oct 2025 / Optics Express 44345

Optics EXPRESS

Efficient high-power continuous-wave multi-slab Fe:ZnSe laser at 4.1 μm

NoSoung Myoung,[1,*] Sangmi Na,[1,2] Seong Ku Lee,[1] Jae Hee Sung,[1] Jongwan Kim,[3] Changjun Yoon,[3] and Sergey Mirov[4]

[1]*Advanced Photonics Research Institute, Gwangju Institute of Science and Technology (GIST), Gwangju 61005, Republic of Korea*
[2]*EO/IR Systems R&D, LIG Nex1 Co., Ltd., Yongin-si, Gyeonggi-do 16911, Republic of Korea*
[3]*Electro-Optics System 2 team, Hanwha Systems, Gyeonggi-do 13524, Republic of Korea*
[4]*Department of Physics, The University of Alabama at Birmingham, Birmingham, AL 35233, USA*
[*]*nsmyoung@gist.ac.kr*

Abstract: We report high-efficiency continuous-wave operation of a cryogenically cooled Fe^{2+}:ZnSe laser at 4.167 μm using a four-slab configuration (2.75 mm each, 4.3-7.9 × 10^{18} cm^{-3}) optimized for pump absorption and gain distribution. Cooled to 90 K and double-end pumped at 2.832 μm by two fiber-bulk hybrid Cr:ZnSe lasers (17 W and 13 W), the system achieved complete pump absorption ($\eta_a \approx 99.68\%$), delivering 13.9 W output with 41% slope efficiency. Beam quality was near diffraction-limited (M_X^2 = 1.13 ± 0.11, M_Y^2 = 1.24 ± 0.12). The lasing wavelength red-shifted from 4.036 to 4.167 μm with power, attributed to thermal and gain-spectrum dynamics. This architecture mitigates thermal lensing and supports efficient mid-infrared power scaling.

1. Introduction

Mid-infrared (mid-IR) lasers, spanning the spectral range of approximately 3-5 μm, are of particular interest because of their exceptional suitability for applications in spectroscopy, environmental sensing, medical diagnostics, and laser surgery, as well as in defense systems such as infrared countermeasures (IRCM) and target illumination [1–3]. Many molecular species exhibit strong vibrational transitions in this region, making mid-IR sources ideal for highly selective detection [4]. In medical regimes, the high absorption of mid-IR light in water and biological tissues enables precise and minimally invasive surgical procedures [5,6]. For defense, mid-IR lasers can penetrate obscurants such as smoke and fog, and are crucial for disabling infrared imaging sensors [7,8].

Among the available mid-IR gain media, Fe^{2+}:ZnSe stands out for its broad tunability (3.9 to 5.0 μm), high emission cross-section, and compatibility with direct optical pumping using commercial Er-doped fiber lasers at 2.8 μm [9,10]. These properties make Fe:ZnSe particularly attractive for developing compact, efficient solid-state mid-IR laser sources. However, the development of high-power continuous-wave (CW) Fe:ZnSe lasers remains technically challenging. One of the primary difficulties arises from the relatively short upper-state lifetime at room temperature due to multiphonon relaxation, as well as strong thermal lensing effects induced by heat generation under high-intensity pumping. These thermal effects degrade beam quality, distort resonator stability, and limit achievable output power [11,12]. Cryogenic cooling has emerged as a powerful strategy to mitigate these thermal constraints. Operating Fe:ZnSe at low temperatures significantly suppresses non-radiative losses and extends the upper-state lifetime, thereby enhancing quantum efficiency and gain. In addition, the reduced thermal load and higher thermal conductivity at cryogenic temperatures contribute to better beam quality and higher slope efficiency in CW operation.

#577277 https://doi.org/10.1364/OE.577277
Journal © 2025 Received 3 Sep 2025; revised 6 Oct 2025; accepted 7 Oct 2025; published 10 Oct 2025

The first demonstration of CW Fe:ZnSe laser was reported in 2008 [13]. In that study, the authors employed a liquid-nitrogen (LN) cooled Fe:ZnSe single crystal ($N_{Fe} = 2.5 \times 10^{18}$ cm^{-3}, $4 \times 2.5 \times 7.7$ mm) in a non-selective resonator, achieving a maximum output power of 160 mW with a slope efficiency of 56% and an optical-to-optical (OTO) efficiency 26.7% under 0.6 W of 2.97 µm Cr:CdSe laser pumping. One of the major impediments to power scaling of CW Fe:ZnSe lasers was the limited availability of high-power CW pump sources in the 2.6-3.1 µm spectral band. Subsequent progress was achieved in 2012 [14], when CW output was scaled to 840 mW at 77 K in a non-selective cavity using two "Sheaumann Laser" MIR-PAC microchip lasers at 2.94 µm, delivering 3 W of combined pump power. In that experiment, liquid-nitrogen-cooled diffusion-doped polycrystalline Fe:ZnSe ($N_{Fe} = 9.8 \times 10^{18}$ cm^{-3}, $5 \times 8 \times 2.5$ mm, by IPG Photonics) yielded an OTO efficiency of 39%. Further development in 2015 [15] with a 10 W Er:Y_2O_3 pump laser at 2.74 µm resulted in 794 mW of Fe:ZnSe output under 8.2 W of absorbed pump, albeit with a reduced OTO efficiency of ~10%. More recently, in 2021, the use of a CW Er:YAP laser at 2.92 µm for pumping a liquid-nitrogen-cooled Fe:ZnSe single crystal ($N_{Fe} = 2.2 \times 10^{18}$ cm^{-3}, $4 \times 2 \times 8$ mm) enabled scaling the CW output to 1 W, with an OTO efficiency of 28% [16]. Advances in ~3 µm Er-doped fluoride fiber lasers have played a pivotal role in enabling further power scaling of CW Fe:ZnSe lasers [17]. In 2018, a compact CW laser based on a single Fe:ZnSe crystal ($N_{Fe} = 3.5 \times 10^{18}$ cm^{-3}, $10 \times 10 \times 8.5$ mm) was demonstrated under pumping by an Er:ZBLAN fiber laser at 2.8 µm, yielding a maximum output power of 2.1 W with an optical-to-optical (OTO) efficiency of 32% [10]. More recently, in 2024, the output power of an Er:ZBLAN fiber-pumped Fe:ZnSe laser at 2.907 µm was scaled to 5.5 W with an OTO efficiency of 54.5% [18]. In this work, a single Fe:ZnSe crystal ($N_{Fe} = 5.5 \times 10^{18}$ cm^{-3}, $7 \times 7 \times 9$ mm) was employed, and a non-selective cavity was realized using mirrors directly deposited on the crystal facets.

Progress in room temperature, tunable over 1.9-3.0 µm, high power CW Cr:ZnS/Se master oscillator power amplifier (MOPA) systems, based on both slab [19] and spinning ring gain elements [20–22], has provided effective pump sources for Fe:ZnSe lasers. In 2015 [4], CW Fe:ZnSe output in a nonselective cavity was scaled up to 1.6 W under 4.8 W of 2.75 µm pump radiation of Cr:ZnS MOPA. LN cooled diffusion doped polycrystalline Fe:ZnSe ($N_{Fe} = 1.5 \times 10^{19}$ cm^{-3}, $5 \times 8 \times 2.5$ mm, by IPG Photonics] was utilized, and the OTO efficiency of lasing with regard to the pump power was ~30%. Importantly, no indication of thermal rollover was observed, and the output power was limited solely by the available pump power. In a subsequent study, a simple linear dispersive cavity was implemented using a plane high reflector, two lenses, and a diffraction grating in Littrow configuration. By varying the Fe:ZnSe gain element temperature between 77-170 K, wavelength tunability across the 3700-4950 nm range was achieved. The optimal temperature for both maximum tuning bandwidth and output power was found to be approximately 140 K, where a maximum output of 0.5 W at 4.1 µm was realized with an OTO efficiency of 12%. The output beam exhibited narrow-linewidth operation (<0.8 nm) in the TEM_{00} mode with beam quality $M^2 < 1.1$.

In 2017, the use of a spinning-ring Cr:ZnSe laser operating at 2.94 µm with an output power of 23 W [21,22] enabled the demonstration of a CW Fe:ZnSe laser that, at the time, achieved the highest reported output power for this class of devices [23]. In that work, a linear, non-selective cavity incorporating AR-coated, LN-cooled, diffusion-doped Fe:ZnSe polycrystals ($N_{Fe} = 1.5 \times 10^{19}$ cm^{-3}, $5 \times 8 \times 2$ mm, by IPG Photonics) placed at normal incidence produced a maximum output of 9.2 W with an optical-to-optical efficiency of ~40%. However, as pump power increases, even cryogenically cooled single-slab designs inevitably encounter limitations imposed by internal thermal gradients and stress-induced degradation.

To overcome these limitations, a multi-slab laser architecture, well-established in high-power Nd:YLF and Nd:YAG solid-state lasers, offers a promising path forward. In such systems, the gain medium is divided into multiple thin slabs, each individually cooled and pumped, enabling more uniform thermal distribution and reduced optical distortion [24]. By adopting a similar strategy in a cryogenic Fe:ZnSe laser, thermal lensing can be significantly reduced, and stress-induced refractive index variations from thermal gradients can be minimized. This enables greater power scalability and stable, high-efficiency operation [25]. Moreover, the use of multiple slabs with tailored doping levels further enables spatial gain optimization and efficient pump absorption, a technique successfully demonstrated in multi-slab Nd:YLF systems for beam combination and amplification [26].

In this work, we demonstrate the first high-power CW Fe^{2+}:ZnSe laser employing four cryogenically cooled gain slabs with tailored dopant concentrations, arranged to optimize pump absorption and gain distribution under a double-end-pumping scheme. By adapting multi-slab thermal-management principles, well established in high-power Nd-doped solid-state lasers, to the mid-infrared Fe^{2+}:ZnSe system, we achieve efficient double-end pumping, uniform gain distribution, and strong mitigation of thermal lensing, enabling scalable and stable CW operation. The following section describes the fabrication of the Fe^{2+}:ZnSe gain elements, the multi-slab resonator design, and the methodology used to characterize the laser's optical performance.

2. Experimental setup

2.1. Sample preparation

The Fe^{2+}:ZnSe gain elements were fabricated using a post-growth thermal diffusion method, a standard technique for incorporating transition-metal (TM) dopants into II-VI semiconductor hosts for mid-infrared laser applications. Polycrystalline ZnSe substrates (10×10 mm) were employed due to their cost-effectiveness and suitability for large-area doping. To enhance dopant adhesion and achieve precise control over surface dopant loading, a thin iron (Fe) film was deposited on the ZnSe surface using an off-axis radio-frequency (RF) magnetron sputtering system. The sputtering was performed in an argon environment with a gas flow rate of 28 sccm. The RF plasma was maintained at a power level of 40 W, and the working pressure was held at 60 mTorr. Under these conditions, the deposition rate of Fe was approximately 0.6 nm per minute, allowing for fine control of the film thickness and, consequently, the dopant concentration.

Following Fe deposition, thermal diffusion was carried out to incorporate Fe^{2+} ions into the ZnSe crystal lattice. The samples were sealed in evacuated quartz ampoules under vacuum ($<10^{-5}$ Torr) and annealed at 980 °C for a duration of 30 days. These extended high-temperature conditions ensured deep and uniform dopant diffusion. By varying the initial Fe film thickness and carefully controlling the diffusion process, the dopant concentrations from 4.3 to 7.9×10^{18} cm^{-3} were achieved and used to fabricate separate slabs for integration into a multi-slab laser structure. The resulting Fe:ZnSe crystals were optically polished into 2.75 mm-thick slabs on both surfaces for laser cavity integration. To minimize Fresnel losses and ensure high transmission for both pump and laser wavelengths, all Fe:ZnSe slabs were coated with a custom dual-band anti-reflection (AR) coating. The coating was designed to provide high transmission in the mid-infrared range from 3800 nm to 5000 nm (corresponding to the laser emission band), as well as at the pump wavelength of 2832 nm. This dual-band AR coating facilitated efficient pump absorption and laser extraction with minimal reflection losses.

2.2. Multi-slab configuration and laser cavity

To achieve efficient and balanced pump absorption in the double-end-pumped configuration, four Fe:ZnSe slabs, each with a thickness of 2.75 mm and with different dopant concentrations (4.3, 4.56, 6.8, and 7.9×10^{18} cm^{-3}) were strategically arranged along the optical axis maintaining a 0.5 mm uniform separation between each element individually wrapped with indium foil to ensure effective thermal management and mechanical stability shown in Fig. 1. The slabs with the lowest Fe concentrations (4.3×10^{18} and 4.56×10^{18} cm^{-3}) were placed at the ends of the gain medium stack, where the incident pump intensity is highest, while the more highly doped slabs (6.8×10^{18} and 7.9×10^{18} cm^{-3}) were positioned near the center, where the pump power is attenuated. The assembled multi-slab structure was enclosed within a precision-machined copper housing, which served as both a mechanical fixture and a thermal conductor. This spatial doping profile was designed to equalize pump absorption per slab, mitigate thermal gradients, and maintain a more uniform inversion distribution, ultimately supporting stable CW laser operation at cryogenic temperature.

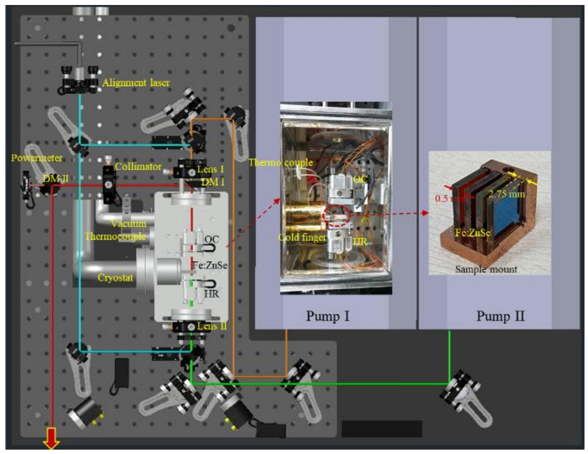

Fig. 1. Schematics of multi-slab Fe:ZnSe laser.

The entire assembly was maintained at a cryogenic temperature of 90 K under vacuum conditions ($<10^{-6}$ Torr) to minimize thermal load and improve the spectroscopic performance of the Fe:ZnSe gain medium. Cooling was achieved using a closed-cycle cryocooler from CryoSpectra (Austria), delivering up to 75 W of cooling capacity at 90 K with ultra-low vibration operation and compact cold heads specifically designed for laser applications. The gain medium was optically excited using a double-end pumping scheme implemented with two identical pump lasers. Each pump source was a CW fiber-bulk hybrid Cr:ZnSe laser operating at a central wavelength of 2832 nm, provided by IPG Photonics. This wavelength was well-matched to the absorption band of Fe:ZnSe, ensuring efficient energy transfer into the upper laser level. The fiber-bulk hybrid architecture enabled high beam quality and stable power delivery, making it particularly suitable for cryogenically cooled, high-efficiency mid-infrared solid-state laser operation. Moreover, as shown in [27], the cross-section of Fe:ZnSe absorption is constant over the 78-340 K temperature range, making it convenient for a comparative study of Fe:ZnSe lasing at different temperatures.

The laser cavity was formed by a plano-concave resonator. The high-reflectivity (HR, CaF_2) mirror exhibited high transmission at the pump wavelength of 2832 nm and high reflectivity (R $\approx$ 99.0%) over the lasing band of 3.9~4.5 µm. The output coupler (OC, CaF_2) was a concave mirror with a radius of curvature (ROC) of 50 mm, designed with high transmission at 2832 nm to pass the pump and ~45% transmission at ~4.0 µm for efficient laser extraction. To minimize intracavity losses, both the HR and OC were placed inside the vacuum chamber together with the gain medium. This configuration eliminates the need for additional intracavity CaF_2 windows, which-even with high-quality AR coatings-would otherwise contribute ~1-2% round-trip loss through residual reflections and absorption in the mid-IR. By avoiding these losses, the total passive round-trip loss was kept below ~1%, thereby reducing threshold pump power and improving slope efficiency. For precise alignment under cryogenic conditions, both the HR and OC mirrors were mounted on vacuum-compatible piezoelectric linear stages providing independent x–y–z translation. This arrangement allowed sub-micron positioning of the cavity mirrors without breaking vacuum, ensuring optimal cavity stability and reliable mode matching with the pump beams. The integration of piezo stages also minimized sensitivity to thermal contraction upon cooldown.

The pump beams from the two Cr:ZnSe sources were focused into the gain module using AR-coated CaF_2 lenses (f = 200 mm). This focal length was selected to match the intracavity mode size defined by the 50 mm ROC output coupler, thereby ensuring strong spatial overlap between the pump volume and the fundamental resonator mode. The pump radiation from each Cr:ZnSe source was focused using a CaF_2 lens (f = 200 mm) and then directed into the gain region by a dichroic mirror (DM I, T ≈ 95% at 2832 nm, R ≈ 99% at 3900-4500 nm). The focused pump beams excited the multi-slab Fe:ZnSe gain medium, while the generated laser emission was reflected by DM I. The output laser beam was subsequently collimated with a CaF_2 lens (f = 200 mm) to a diameter of ~10 mm. Finally, the collimated beam was reflected by a second dichroic mirror (DM II), which separated the mid-IR laser emission from residual pump light, and the transmitted output power was measured at this stage. This optical configuration optimized overlap efficiency between the pump and cavity modes while minimizing Fresnel losses at the AR-coated surfaces. The careful matching of pump beam size to the resonator mode was essential for maximizing absorption efficiency, gain uniformity, and ultimately, slope efficiency in CW operation. The pump and laser beams entered and exited the vacuum chamber through wedged CaF_2 windows with dual-band AR coatings (high transmission at 2.83 μm and 3.9~4.5 μm) combined with the ~3° pump-beam tilt and dichroic mirror arrangement. The wedged geometry effectively suppressed parasitic back-reflections and etalon effect, thereby minimizing optical feedback to the Cr:ZnSe pump lasers and contributing to stable double-end pumping operation.

3. Results and discussion

To optimize pump absorption and thermal distribution within the multi-slab Fe:ZnSe laser configuration, four gain elements were prepared with varying Fe dopant concentrations. The Fe^{2+} concentrations of the four slabs were determined from absorption measurements at the pump wavelength of 2832 nm, using an absorption cross section of $\sigma_{abs} = 0.885 \times 10^{-18}$ cm^2. From these values, the dopant concentrations were calculated as 4.3, 7.9, 6.8, and 4.56×10^{18} cm^{-3} for Slabs 1 through 4, respectively (see Table 1). The corresponding absorption coefficients were measured as 3.82, 7.02, 6.02, and 4.03 cm^{-1}, confirming the strong correlation between doping level and pump absorption strength. Using the Beer-Lambert law, the single-pass absorption for each slab was calculated as 65.0%, 85.7%, 81.1%, and 67.5% for Slabs 1 through 4, respectively. These values confirm that the inner slabs, having higher dopant concentrations, are more effective at capturing the remaining pump light, while the outer slabs provide initial high-efficiency absorption at both ends in the double-end-pumped geometry.

Table 1. Absorption parameters for each slab

Slab	Absorption coefficient [cm^{-1}]	Dopant concentration [×10^{18}, cm^{-3}]	Single-pass absorption	Absorbed by pump I [W]	Absorbed by pump II [W]	Total absorbed [W]
Slab 1	3.82	4.3	0.65	11.05	0.07	11.13
Slab 2	7.02	7.9	0.85	5.08	0.70	5.78
Slab 3	6.02	6.8	0.81	0.69	3.47	4.17
Slab 4	4.03	4.56	0.67	0.11	8.70	8.81

Dividing the Fe:ZnSe gain medium into four cryogenically cooled slabs effectively redistributes the thermal load and reduces local heat density. The maximum absorbed power per slab was 11.13 W (for Slab 1), corresponding to an average heat flux of approximately 10.1×10^7 W/m^2 over the pumped area. On the other hands, a single-slab configuration with equivalent total absorption (~29.9 W) would experience a concentrated peak-local absorbed power of about 15~16 W, leading to a heat flux exceeding 14.1×10^7 W/m^2 near the pump entrance. Thus, the multi-slab configuration lowers the maximum heat flux by nearly 30%, flattens the thermal gradient, and significantly mitigates thermal lensing. This redistribution of absorbed power where outer slabs absorb the initial high intensity pump and inner slabs capture residuals ensures a more uniform temperature and gain profile along the cavity axis.

This strategic arrangement balances total pump absorption and thermal load distribution, ultimately supporting high-power CW laser operation. The total incident pump power was 30 W, with 17 W delivered from pump I and 13 W from pump II. Due to limitations in available pump power, an asymmetric pump configuration was adopted. While symmetric pumping is generally preferred for balanced gain and heat distribution, this asymmetric arrangement was necessary to utilize the maximum available power from both sources. Despite the imbalance, the double-end geometry ensured sufficient absorption in all slabs and helped maintain efficient excitation throughout the gain medium. Although direct wavefront measurements were not conducted, thermal-lens modeling based on standard Gaussian heat-load analysis indicates that the four-slab configuration reduces the maximum lensing strength by approximately 30% compared to a single-slab element. The corresponding focal length increases ~62 mm (single-slab) to ~87 mm (multi-slab) at 90 K, consistent with the observed near diffraction limited beam quality ($M^2 \approx 1.2$) in Fig. 3 and linear power scaling.

Although the four-slab Fe:ZnSe laser achieved nearly complete total pump absorption, the absorbed power distribution remains slightly asymmetric, with Slabs 1 and 4 (outer elements) absorbing a larger fraction of the incident pump compared to the inner slabs. This imbalance results primarily from the combined effects of asymmetric double-end pumping (17 W + 13 W) and the specific Fe concentration gradient used in this study. While a perfectly balanced absorption profile is theoretically desirable to equalize the thermal load, the current configuration was deliberately optimized to ensure complete pump depletion and reduced heating near the cavity center. The excellent beam quality ($M^2 \approx 1.2$) and linear output scaling with no observed thermal saturation indicate that the residual imbalance does not degrade performance. Future designs may employ refined doping gradient or balanced pump powers to further homogenize the absorbed energy distribution, which could lead to even greater scalability and improve long-term thermal stability. Based on the experimentally determined absorption coefficients and slab geometry, the single-pass absorption for each slab varied significantly, with outer slabs (Slab 1 and Slab 4) absorbing the majority of the pump light due to their interaction with the incident beams. Specifically, Slab 1 absorbed 11.05 W from pump I, while Slab 4 absorbed 8.71 W from pump II, demonstrating the dominant role of the pass interaction in pump absorption. In the current configuration, Slabs 2 and 3 (positioned in the center of the cavity) exhibit the highest single-pass absorption approximately 85.7% and 81.1%, respectively, while Slabs 1 and 4 (located at the outer ends) have lower single-pass absorption of 65.0% and 67.0%. This arrangement aligns with the spatial distribution of the incident pump power and ensures strong population inversion within the central gain region. In addition, this balance allows the high-absorption slabs in the center to contribute effectively to gain generation, while the outer slabs capture and utilize the initial high pump intensities.

To evaluate the laser performance potential of the multi-slab Fe:ZnSe system, the theoretical output power of the multi-slab Fe:ZnSe laser system was calculated using a power-scaling model based on absorbed pump power, cavity losses, and gain saturation, as detailed in [6]. The model

Optics EXPRESS

assumes that the slope efficiency η_{slope} (product of individual efficiency terms) governs the conversion of pump power above threshold into output laser power in Table 2.

Table 2. Energy transfer efficiencies in the four-slab configuration

Transfer process	Values
Absorption efficiency, η_a	0.9968
Radiative quantum efficiency, η_{rad}	0.993897
Quantum efficiency, η_Q	0.69073
Upper-state efficiency, η_{up}	0.7722
Coupling efficiency, η_C	0.9782
Beam overlap efficiency, η_B	0.998213

The theoretical slope efficiency was determined to be 51.6% in Fig. 2. With a total absorbed pump power of 29.9 W and a threshold absorbed power of 0.698 W, the corresponding theoretical output power was estimated to be approximately 15.1 W. In comparison, the experimental output power was 13.9 W with an observed slope efficiency of 41%.

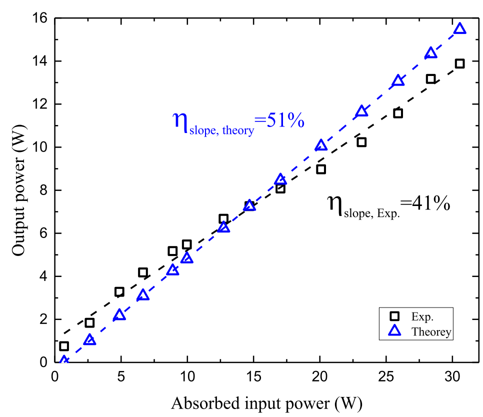

Fig. 2. Input vs. output characteristics of four-slab Fe:ZnSe laser.

The data are linear up to the highest absorbed power (~29.9 W) with no observable roll-off, yielding an experimental slope efficiency of ~41%. The linearity and absence of saturation at maximum drive are consistent with the very high pump-absorption efficiency ($\eta_a \approx 0.9968$) and excellent spatial overlap ($\eta_B \approx 0.998$), together with cryogenic operation (90 K) that minimizes non-radiative quenching ($\eta_{rad} \approx 0.994$). In this configuration, the four slabs distribute the pump and heat load, so the inversion in each plate remains below the saturation regime, and the high output-coupler setting ($T_C = 45\%$) keeps intracavity photon density moderate, preventing gain clamping. As a result, the gain medium behaves nearly linearly in the explored range, and no thermal or ESA-induced rollover is evident.

The theoretical slope efficiency (51.6%) slightly exceeds the measure value (41%). This difference can be explained by a combination of effects not fully captured by the nominal parameters in Table 2: 1) stronger excited-state absorption or residual reabsorption at 4.1 μm, which lowers the effective upper-state efficiency; 2) additional intracavity losses from multiple AR-coated interfaces, dichroic mirrors, and CaF_2 optics; and 3) mild pump-mode overlap degradation at power due to thermal lensing (or aberrations) and small spectral detuning of the pump. A back-calculation show that the measured slope corresponds to an effective multiplicative shortfall of ~0.79 relative to the nominal product, consistent with the combined impact of these mechanisms . Future work will include direct measurement of round-trip loss and ESA at 90 K, and output-coupler optimization to further close the difference.

The spatial beam quality of the four-slab Fe:ZnSe laser was characterized by measuring the beam propagation factor M^2 in accordance with the ISO 11146 standard in Fig. 3. The measurement was performed by recording the beam radius at multiple axial positions along the propagation direction using a mid-infrared beam profiling system (WinCamD-IR-BB, DataRay Inc.) and a ZnSe lens with 150 mm for focusing. The measured beam quality factors were $M_X^2 = 1.13 \pm 0.11$ in the horizontal direction and $M_Y^2 = 1.24 \pm 0.1$ in the vertical direction, indicating near-diffraction-limited performance in both axes. The corresponding far-field intensity distribution exhibited a smooth Gaussian profile without significant astigmatism or ellipticity, confirming excellent mode matching between the pump beam and the laser cavity mode. These results demonstrate that the multi-slab configuration, combined with cryogenic cooling, can deliver high beam quality while operating in a high-power CW regime in the mid-infrared.

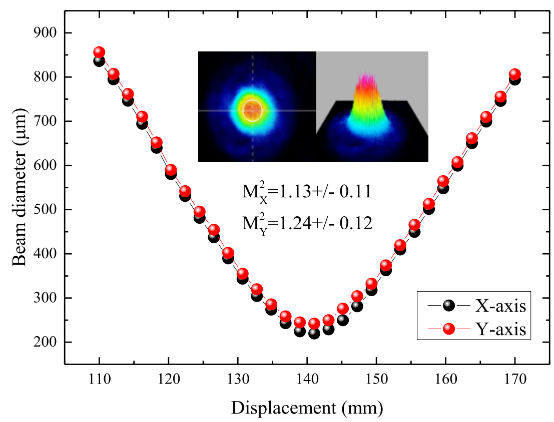

Fig. 3. Measured beam profile of four-slab Fe:ZnSe laser.

Lasing spectra were recorded at three output power levels (100 mW, 5 W, and 10 W) revealing emission peaks at 4036 nm, 4092 nm, and 4167 nm, respectively in Fig. 4. The lasing spectra were recorded using a monochromator with a 150 mm focal length and a 150 grooves/mm grating blazed at 3 µm. Due to the limited dispersion of this configuration (≈1~3 nm resolution at 4 µm), individual longitudinal modes were not spectrally resolved, resulting in a smooth spectral envelope rather than discrete mode peaks. Nevertheless, this spectral resolution was sufficient to accurately determine the central lasing wavelength and to monitor the power-dependent redshift from 4.036 µm to 4.167 µm observed at higher output powers.

The progressive redshift of the lasing wavelength with increasing output power is a well-known characteristic of Fe:ZnSe lasers and can be attributed primarily to thermal effects and gain spectrum dynamics. As the pump power increases, residual non-radiative relaxation processes deposit heat into the gain medium, even under cryogenic operation. This localized heating alters the crystal's refractive index (thermo-optic effect) and slightly changes the Fe^{2+} absorption and emission cross-section spectra, shifting the peak gain toward longer wavelengths. In Fe:ZnSe polycrystals, inhomogeneous broadening arising from variations in local crystal field environments and grain boundaries further enhances the sensitivity of the gain spectrum to temperature.

Additionally, increased population inversion at higher pump powers leads to gain saturation at shorter wavelengths and preferential amplification of longer-wavelength modes that remain unsaturated. This spectral pulling effect, combined with temperature-dependent Stark level

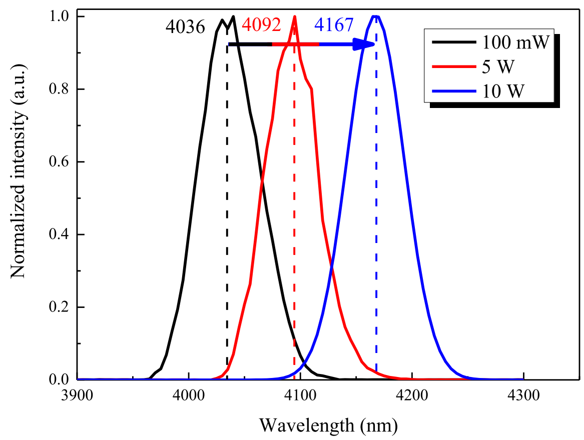

Fig. 4. Lasing spectra in terms of output power.

population redistribution, accounts for the observed ~131 nm total redshift across the studied power range. Similar trends have been reported in other transition-metal-doped II-VI mid-infrared lasers, particularly under high-power CW operation [14,28], where even small residual thermal loads can significantly shift the lasing wavelength within the broad Fe:ZnSe emission band. Likewise, Pushkin et al. documented continuous tuning of the central wavelength from 4012 to 4198 nm as pump power and iron-ion doping increased in a mid-IR Fe:ZnSe laser, which aligns closely with our observations [10].

4. Conclusions

A cryogenically cooled, four-slab Fe^{2+}:ZnSe laser with tailored doping and double-end pumping achieved a world-record CW output power of 13.9 W at 4.167 µm, with a slope efficiency of 41% and near diffraction-limited beam quality. The measured performance closely matched theoretical predictions (51.6% slope efficiency) and exhibited no saturation up to the maximum absorbed pump power of 29.9 W, confirming the effectiveness of the multi-slab architecture in balancing pump absorption, thermal load, and gain distribution. A power-dependent redshift of the emission wavelength from 4036 to 4167 nm was observed, consistent with thermal effects and gain-spectrum dynamics. These results demonstrate that cryogenic multi-slab Fe^{2+}:ZnSe lasers provide a robust and scalable platform for realizing high-power, high-beam-quality CW mid-infrared sources. Further power scaling can be anticipated through the use of additional gain slabs, higher pump power density, or improved heat extraction designs such as conduction cooled or actively temperature-controlled slab mounts. The demonstrated architecture also provides a foundation for implementing mode-combined or MOPA configurations, opening a pathway toward tens of watts class CW Fe:ZnSe systems for spectroscopy, medical, and defense applications.

Funding. Defense Acquisition Program Administration (UC200013D); National Research Foundation of Korea (NRF-2020R1I1A1A01051794, NRF-2017R1D1A1B03031753); Gwangju Institute of Science and Technology (Future-Leading Specialized Research Project grant).

Acknowledgments. The work was supported by Defense Rapid Acquisition Technology Research Institute (DRATRI) – Grant funded by Defense Acquisition Program Administration (DAPA, UC200013D), Basic Science Research Program through the National Research Foundation of Korea (NRF) funded by the Ministry of Education (NRF-2020R1I1A1A01051794 and NRF-2017R1D1A1B03031753), and Future-Leading Specialized Research Project grant funded by the GIST in 2025.

Disclosures. The authors declare no conflicts of interest.

Optics EXPRESS

Data availability. Data underlying the results presented in this paper are not publicly available at this time but may be obtained from the authors upon reasonable request.

References

1. M. A. Butt, M. Juchniewicz, M. Słowikowski, *et al.*, "Mid-Infrared Photonic Sensors: Exploring Fundamentals, Advanced Materials, and Cutting-Edge Applications," Sensors **25**(4), 1102 (2025).
2. M. R. Majewski, R. I. Woodward, and S. D. Jackson, "Dysprosium mid-infrared lasers: Current status and future prospects," Laser Photonics Rev. **14**(3), 1900195 (2020).
3. F.K Tittel, D. Richter, and A. Fried, "Mid-Infrared Laser Application in Spectroscopy," in *Solid-State Mid-Infrared Laser Sources* pp. 445–497 (Springer, 2008).
4. M. W. Sigrist, "Trace gas monitoring by laser photoacoustic spectroscopy and related techniques," Rev. Sci. Instrum. **74**(1), 486–490 (2003).
5. A. Vogel and V. Venugopalan, "Mechanisms of pulsed laser ablation of biological tissues," Chem. Rev. **103**(2), 577–644 (2003).
6. I. K. Ilev and R. W. Waynant, "Mid-infrared Biomedical Applications," in *Mid-infrared Semiconductor Optoelectronics* 118, pp. 615–634 (Springer, 2006).
7. H. H. P. Bekman, J. C. van den Heuvel, F. J. M. van Putten, *et al.*, "Development of a Mid-Infrared Laser for Study of Infrared Countermeasures Techniques," Proc. SPIE **5615**, 27–38 (2004).
8. L. J. Cox, M. A. Batten, S. R. Carpenter, *et al.*, "Modeling countermeasures to imaging infrared seekers," Technologies for Optical Countermeasures, Proc. SPIE **5615**, 112–119 (2004).
9. R. Švejkar, J. Šulc, M. Němec, *et al.*, "Compact diode-pumped CW and Q-switched 2.8 µm Er:YLF laser," J. Opt. Soc. Am. B-Opt. Phys. **38**(8), B26–B29 (2021).
10. A. V. Pushkin, E. A. Migal, H. Uehara, *et al.*, "Compact, highly efficient, 2.1-W continuous-wave mid-infrared Fe:ZnSe coherent source, pumped by an Er:ZBLAN fiber laser," Opt. Lett. **43**(24), 5941–5944 (2018).
11. W. Koechner, *Solid-State Laser Engineering* 6th ed. pp.102–126 (Springer, 2006).
12. R. Weber, B. Neuenschwander, and H. P. Weber, "Thermal effects in solid-state laser materials," Opt. Mater. **11**(2-3), 245–254 (1999).
13. A. A. Voronov, V. I. Kozlovsky, Y. V. Korostelin, *et al.*, "A continuous-wave Fe^{2+}:ZnSe laser," Quantum Electron. **38**(12), 1113–1116 (2008).
14. J. W. Evans, P. A. Berry, and L. L. Schepler, "840 mW continuous-wave Fe:ZnSe laser operating at 4140 nm," Opt. Lett. **37**(23), 5021–5023 (2012).
15. J. W. Evans, T. Sanamyan, and P. A. Berry, "A continuous wave Fe:ZnSe laser pumped by efficient Er:Y_2O_3 laser," Proc. SPIE **9342**, 93420F (2015).
16. E. Li, H. Uehara, W. Yao, *et al.*, "High-efficiency, continuous-wave Fe:ZnSe mid-IR laser end pumped by an Er:YAP laser," Opt. Express **29**(26), 44118 (2021).
17. Y. O. Aydin, V. Fortin, R. Vallée, *et al.*, "Towards power scaling of 2.8 µm fiber lasers," Opt. Lett. **43**(18), 4542–4545 (2018).
18. Y. Shen, Y. Wan, F. Zhu, *et al.*, "High-power compact continuous-wave Fe:ZnSe laser at 4 µm with >50% overall conversion efficiency," Chin. Opt. Lett. **22**(8), 081405 (2024).
19. S. Mirov, V. Fedorov, D. Martyshkin, *et al.*, "Progress in Mid-IR Lasers Based on Cr and Fe Doped II-VI Chalcogenides," IEEE J. Sel. Top. Quantum Electron. **21**(1), 292–310 (2015).
20. S. Mirov, V. Fedorov, D. Martyshkin, *et al.*, "High Average Power Fe:ZnSe and Cr:ZnSe Mid-IR Solid State Lasers," Advanced Solid State Lasers, paper AW4A.1 (Optica Publishing Group, 2015).
21. I. Moskalev, S. Mirov, M. Mirov, *et al.*, "140W Cr:ZnSe laser system," Opt. Express **24**(18), 21090–21104 (2016).
22. S. Mirov, I. Moskalev, S. Vasilyev, *et al.*, "Frontiers of mid-IR lasers based on transition metal doped chalcogenides," IEEE J. Sel. Top. Quantum Electron. **24**(5), 1–29 (2018).
23. D. V. Martyshkin, V. V. Fedorov, M. Mirov, *et al.*, "High power (9.2 W) CW 4.15 µm Fe:ZnSe laser," in *Conference on Lasers and Electro-Optics*, STh1L.6 (2017).
24. Z. Ma, J. Gao, D. Li, *et al.*, "Thermal stress effects of the diode-end-pumped Nd:YLF slab," Opt. Commun. **281**(13), 3522–3526 (2008).
25. X. Fu, P. Li, Q. Liu, *et al.*, "3 kW liquid–cooled elastically-supported Nd:YAG multi-slab CW laser resonator," Opt. Express **22**(15), 18421–18432 (2014).
26. J. Chang, Q. Bian, Y. Bo, *et al.*, "2.85-kW cryogenic Nd:YAG slab laser operating at 946 nm," Front. Phys. **11**, 1–5 (2023).
27. A. Riha, H. Jelinkova, M. E. Doroshenko, *et al.*, "Temperature dependence of Fe:ZnSe mid-infrared spectral and laser output properties under ~4 µm radiation excitation," J. Opt. Soc. Am. B **41**(12), E8–E14 (2024).
28. D. Martyshikin, K. Karki, V. Fedorov, *et al.*, "Room temperature, nanosecond, 60mJ/pulse Fe:Znse master oscillator power amplifier system operating at 3.8-50 µm," Opt. Express **29**(2), 2387–2393 (2021).